Real-Time Estimation of Electron Mobility in Hall Effect Thruster Models

IEPC-2022-342

Presented at the 37th International Electric Propulsion Conference
Massachusetts Institute of Technology, Cambridge, MA, USA
June 19-23, 2022

Christine M. Greve[1]
Texas A&M University, College Station, TX 77843, USA

Kentaro Hara[2]
Stanford University, Stanford, CA 94305, USA

An extended Kalman filter (EKF) is used to estimate unknown parameters in one-dimensional models, with the goal of estimating the electron mobility coefficients within real time in Hall effect thruster models. The estimator predicts the time history of unknown states based on knowledge of the plasma dynamics coupled with experimental measurements. Numerical examples such as heat advection and thermal conduction demonstrate the effectiveness of the extended Kalman filter with one-dimensional models before initial applications to a Hall effect thruster case to estimate electron mobility parameters. While the extended Kalman filter is able to reasonably estimate the two simple cases of linear advection and thermal diffusion, the application to the Hall effect thruster model proves riddled with numerical artifacts and highly sensitive physical relations.

I. Nomenclature

A = thruster inlet area
B = magnetic field
E = electric field
e = elementary charge
f = physics-based propagation scheme
$\boldsymbol{h}$ = observation function
I = identity matrix
I_d = discharge current
j_d = net current density
K = Kalman gain
k_B = Boltzmann constant
L_{ch} = length of the channel
m_i = mass of ion
m_e = mass of an electron
N_i = number density of ions
N_n = number density of neutrals
n_e = number density of electrons
P = covariance matrix

---

[1] Ph.D. Graduate. Department of Aerospace Engineering. cgreve@tamu.edu
[2] Assistant Professor. Department of Aeronautics and Astronautics. kenhara@stanford.edu

p = pressure or electrons, subscript e, or ions, subscript i
R_k = measurement noise covariance
T_e = electron temperature
t = time
u_e = electron velocity in the x or y directions
V_a = anode sheath potential
$\boldsymbol{x}$ = state vector
$\boldsymbol{y}$ = measurement signal vector
Γ = electron e or ion i flux
$\mu_{e,\perp}$ = cross-field electron mobility
ν_m = momentum transfer collision frequency
Ω = Hall parameter
ω_B = electron gyrofrequency
ϕ = electric potential

II. Introduction

While Hall effect thrusters (HETs) offer enticing advantages for deep-space missions, their use remains limited due to poorly understood lifespan limiting phenomena. Computational models have not yet surpassed ground testing in predictive capabilities, meaning that the most reliable data are come from experimental work which may suffer from limited data acquisition rates and intrusive measurement techniques. In part, these limitations have hindered the growth of computational models into truly predictive models that encapsulate the complex temporal and spatial dynamics of plasma processes. Further use and development of HET technology hinges on the development of reliable, predictive models to advance designs and provide on-board control capabilities by better understanding thruster lifespan limiters.

To this end, a variety of physics-based models have been developed to replicate complex physics, ranging from kinetic simulations that capture non-Maxwellian effects to fluid models that use device-scale calculations using simplified electron transport dynamics, such as drift-diffusion models [1–5]. Research with these models continue to develop increasingly high-fidelity models that have high computational costs. Separately, recent advances in data-driven modeling are providing new research opportunities for the use of lower-fidelity models supplemented with experimental data. The ability to use experimental data to uncover the time histories of non-observed quantities also enables a robust calculation setup that allows for estimation of the state in real time, e.g., on-board a spacecraft. A cursory approach to such data-driven modeling approaches has been performed using sparse regression techniques with an HET model and sparse identification for fluid vortex shedding [6, 7]. Recently, Greve et al. have developed an automated model calibration framework using the Wasserstein metric [8].

This work aims to use an extended Kalman filter (EKF) in conjunction with a one-dimensional (1D) Hall effect thruster model to estimate the time histories of unknown states and parameters such as electron mobility coefficients. While state estimation techniques have been used in artificial intelligence, navigation, and fault detection, their application to plasma physics is not widely reported in literature. In previous work, Greve et al. developed a physics-constrained EKF to model low-frequency plasma oscillations in Hall effect thrusters and pulsed plasma modes in inductively coupled plasmas using a zero-dimensional (0D) global model with simplified plasma chemistry [9]. This work presents incremental testing of the EKF to demonstrate its effectiveness with particle drift through a linear advection testcase in section (IV), and diffusion through a thermal diffusion study in section (V). The results of these simple one-dimensional studies are applied to a one-dimensional quasineutral drift-diffusion Hall effect thruster model in section (VI), revealing the challenges of this data-driven modeling technique.

III. Development of a State Estimation Method

Filtering uses physics-based models in conjunction with time-dependent experimental data. The most accurate state estimation technique is the particle filter, which propagates all possible state trajectories to obtain uncertainties of the model estimation. While accurate, the computational time of these filters can be more expensive than desired. To reduce the computational cost, one can make approximations for the uncertainty distribution such as the Kalman filter, which assumes Gaussian-shaped uncertainties. A further extension of the Kalman filter, known as the extended Kalman filter (EKF), makes use of a Taylor series expansion in the near region of the model to enable the filter to handle moderate nonlinearities.

As derivations of the extended Kalman filter are widely available in literature [10–13], only a brief discussion is presented. In particular, this work is based upon the continuous-discrete extended Kalman filter, analogous to a predictor-corrector scheme. A physics-based model is used to continuously propagate the state estimates and associated covariances, while discrete measurement data points are used to correct the estimation. The predictor step corresponds to temporal evolution of the state vector from $\hat{x}^+_{k-1}$ to $\hat{x}^-_k$ and the corrector step updates $\hat{x}^-_k$ to $\hat{x}^+_k$, where superscript $(-)$ and $(+)$ indicate the estimation before and after the measurement updates, respectively, and k denotes the time step at which data are used to update the state estimates. For notation purposes, the tilde (˜) symbol denotes a measurement, and the hat (ˆ) symbol is an estimate.

The extended Kalman filter can be applied to any general dynamical system of state vector $\boldsymbol{x}(t)$ written as $\dot{\boldsymbol{x}}(t) = \boldsymbol{f}(\boldsymbol{x}(t), t) + G(t)\boldsymbol{\omega}(t)$ where $\boldsymbol{f}$ is the physics-based model, G is a process noise gain matrix, $\boldsymbol{\omega}$ is the process noise, and t is time. The incoming measurements can be written as $\tilde{\boldsymbol{y}}_k = \boldsymbol{h}(\boldsymbol{x}_k) + \boldsymbol{v}_k$ where $\boldsymbol{h}$ is the observation function and $\boldsymbol{v}$ is the zero-mean measurement noise at every discrete time step k, when the measurements are obtained.

The state vector, $\hat{\boldsymbol{x}}$, and covariance (error) matrix, $P(t) = E\{\Delta\boldsymbol{x}\Delta\boldsymbol{x}^T\}$ where $\Delta\boldsymbol{x} = \hat{\boldsymbol{x}}(t) - \boldsymbol{x}(t)$ and E is the expectation, are continuously propagated based on the physics-based model as

$$\dot{\hat{\boldsymbol{x}}}(t) = \boldsymbol{f}(\hat{\boldsymbol{x}}(t), t), \tag{1a}$$

$$\dot{P}(t) = F(\hat{\boldsymbol{x}}(t), t)P(t) + P(t)F^T(\hat{\boldsymbol{x}}(t), t) + G(t)Q(t)G^T(t), \tag{1b}$$

where $F = \partial\boldsymbol{f}/\partial\boldsymbol{x}|_{\hat{\boldsymbol{x}}(t)}$ is the Jacobian matrix of the model function of the system, which allows for a Taylor series expansion of the nonlinear model around the estimated state, and Q is the process noise covariance. When a discrete measurement dataset arrives in time, the Kalman filter corrects the estimate using the discrepancy between the most recent predicted state and the new measurement data. The states and covariances are corrected from the continuous propagation based on the physics-based model, the superscript minus (-), to the updated values, the superscript plus (+), as

$$\hat{\boldsymbol{x}}^+_k = \hat{\boldsymbol{x}}^-_k + K_k\left[\tilde{\boldsymbol{y}}_k - \boldsymbol{h}(\hat{\boldsymbol{x}}^-_k)\right], \tag{2a}$$

$$P^+_k = \left[I - K_k H_k(\hat{\boldsymbol{x}}^-_k)\right]P^-_k, \tag{2b}$$

where $H_k(\hat{\boldsymbol{x}}^-_k) \equiv \partial\boldsymbol{h}/\partial\boldsymbol{x}|_{\hat{\boldsymbol{x}}^-_k}$ is a basis function that denotes the relationship between the measurement and the state vector,

$$K_k = P^-_k H^T_k(\hat{\boldsymbol{x}}^-_k)\left[H_k(\hat{\boldsymbol{x}}^-_k)P^-_k H^T_k(\hat{\boldsymbol{x}}^-_k) + R_k\right]^{-1} \tag{3}$$

is the Kalman gain, and R is the measurement noise covariance. Note that the Kalman gain, determined, by the estimation uncertainties and the measurement noise, is used to adjust the state estimates and covariances, as shown in Eqs. (2a) and (2b).

IV. Linear Advection

This study demonstrates that the EKF can be used to track spatial variations in time, emblematic of electron drift within a Hall effect thruster. The EKF is applied to a one-dimensional linear advection testcase with the goal of recovering the sinusoidal, time-dependent dynamics of the entire domain given a zero-condition initial domain and two measurement locations. As this study indicates the first testcase in one dimension for this work, the following study is a recreation of a test case presented in Ref. 14.

For this case, the state vector is written as $\hat{\boldsymbol{x}} = [\boldsymbol{w}]^T$ where w represents the vector of every cell value in the problem. For this particular test, 120 cells are equally spaced from 0 to 30. The reference solution is created based on the sinusoidal wave propagation equation $w = \sin[2\pi(n\Delta x - t)/\lambda]$, where $t > 0$ is the current time, n is the cell number, $\Delta x = 0.25$ is the cell size, and $\lambda = L/2$ is the wavelength. The initial guess for the state vector is zero for every cell, shown in Fig. 1(a), while the covariances are set as a Gaussian correlation function based on a user-defined folding distance, r_e [14]. The filter is propagated forward in time with a propagation timestep of 0.06, and new measurement data arrive with a timestep of 0.3. The values at cells $x = 5$ and $x = 20$ are used as two measurement signals for this particular case. The model covariance is set constant at $Q = 1$ while the measurement noises for each measured cell are $\sigma_1 = 0.05$ and $\sigma_2 = 0.1$.

Figure 1 shows select snapshots of the EKF estimate after increasing numbers of measurement updates. As seen in Fig. 1(d), the EKF is able to replicate the reference dynamics given a sufficient number of measurement update steps. Figure 1(b) shows how the measurements at $x = 5$ and $x = 20$ not only update those specific cell values, but also the nearby cells across the domain. Figure 1(c) shows the continued improvement of the solution as the reference signal advects before full agreement is reached in Fig. 1(d). The pink uncertainty bounds, calculated from the covariance matrix, P, are shown to diminish as the filter operates due to the incoming measurement data. The increase in uncertainty to the right of the measurement points is a direct consequence of the first-order upwind propagation scheme of the model as the information flows left to right. Note that changing the values of Q and R will change the size and shape of the uncertainty bounds. These initial results demonstrate the capability of the EKF to track spatial trends from few measurement signals, indicating that the EKF will be capable of following particle drift in a plasma simulation.

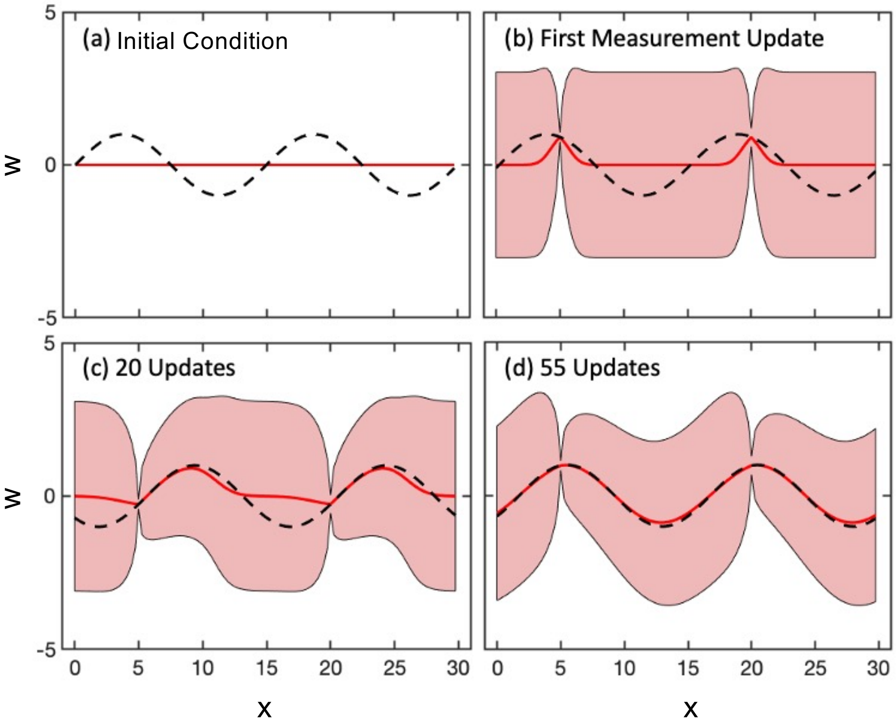

Fig. 1 An example of the EKF updating a linear advection solution (a) at time step $t = 0$, (b) after the first measurement update, (c) after 20 measurement updates, and (d) after 55 measurement updates when the system matches the reference solution. The estimates (red solid line) are shown with their 3σ uncertainty bounds (pink shade) and the reference solution (black dashed line).

V. Thermal Conduction

To study the capabilities of the EKF with diffusion processes, a simple thermal conduction testcase is created. This case requires the EKF to track spatial variation in two directions with limited measurement data. By choosing to estimate the thermal conductivity parameter, κ, this study emulates estimating an electron mobility parameter that affects the motion of electrons in a plasma. Studies have been performed using the EKF to estimate thermal conductivity parameters in other literature [15], but this study will not replicate that work.

A. Numerical Setup

The general thermal conduction equation can be written as $u_t = \kappa u_{xx}$ where the subscripts t and x indicate partial derivatives with respect to time and space, respectively. The double xx subscript indicates a second derivative. The initial condition over 100 cells in a domain of 0 to 1 is set as a discontinuous pulse in the center of the domain, such that

$$\begin{aligned} if(x < 0.4 \text{ or } x > 0.6) &\rightarrow u = 0, \\ if(0.39 < x < 0.61) &\rightarrow u = 1. \end{aligned} \tag{4}$$

For this work, the system is propagated as first order forward in time and second order in space using a central-differencing scheme as shown below

$$\frac{u_{k+1}^{n} - u_{k}^{n}}{\Delta t} = \kappa \frac{u_{k}^{n+1} - 2u_{k}^{n} + u_{k}^{n-1}}{\Delta x^2}, \tag{5}$$

with a thermal conductivity coefficient of 0.7.

The initial condition given to the EKF is a zero-value domain with some assumption for the value of the thermal conductivity coefficient. The state vector consists of the solution at every cell as well as the conductivity coefficient, such that $\boldsymbol{x} = [\boldsymbol{u}\ \kappa]^T$ where $\boldsymbol{u}$ represents the vector of every cell value in the domain. This setup leads to a diagonal Jacobian matrix consisting of the partial derivatives of the propagation equation with respect to the cell of interest, the cell to the right and left of the current cell, and the thermal conductivity coefficient. The covariance matrix is constructed the same way as for the linear advection test case using a set r_e folding scale to initialize the matrix. The propagation is ensured to meet the Von Neumann stability condition as $\kappa \Delta t / \Delta x^2 \leq 1/2$ to prevent numerical instabilities. The EKF uses a time step of $\Delta t = 2.5 \times 10^{-5}$ with a measurement signal of $\Delta t_m = 2.5 \times 10^{-4}$. The process noise covariance is set equal to 1 for every unknown, and the measurement noise covariance is set to 0.01.

B. Estimating One Thermal Conductivity Condition

Part of this work is intended to understand whether the EKF is affected by the presence of time-dependent oscillations during the simulation. This is induced by adding a source term to the original conduction equation such that

$$u_t = \kappa u_{xx} + Q_s, \tag{6}$$

where Q_s is a source term of any functional form or value. For this study, the source term takes the form of a repeating pulse mode to create a steady oscillation, which is motivated by the pulsed ICPs[9]. To enable a truly repeatable pulse, Dirichlet boundary conditions are used for this particular test case. Measurement signals are supplied for $x = 0.45, 0.55$ as it was discovered in previous studies that two measurement signals improved the overall accuracy of the estimate.

Figure 2(a) shows the value of the central cell in the domain to demonstrate effect of the source term, in red, compared to the sourceless diffusion case shown, in black. Note that the pulsed solution is perfectly repeated in each oscillation, but is only shown with one tenth of the original data in this figure, leading to an incomplete figure. Figure 2(b) compares the estimate of a single thermal conductivity coefficient, applied across the entire domain, for both the constant diffusion and the pulsed source term cases. The pulsed solution is seen to overestimate the reference thermal conductivity value of 0.7 as time continues, while the sourceless estimate has reached a near steady-state condition notably closer to the reference solution. These results are the first indication that time-dependent oscillations that affect spatial distributions may be of concern in future applications of the extended Kalman filter. As the system has no knowledge of the pulse prior to the arrival of measurement data, the EKF attempts to account for the oscillations by altering the thermal conductivity coefficient. This incorrect assignment of causation requires further study to determine whether certain limitations could be put on the EKF to improve the estimate.

C. Estimating Two Thermal Conductivity Coefficients

Using the sourceless testcase and increasing the complexity of the unknown physics of the problem, here we aim to demonstrate the capability of the EKF to simultaneously estimate two thermal conductivity coefficients. Studies quickly showed that at least one measurement signal was required in each different section of the domain for observability conditions to be met. Thus, two measurement signals are used to estimate the two thermal conductivity coefficients. The domain is split equally in half with $x \in [0, 0.5]$ using $\kappa_1 = 0.7$ and $x \in [0.5, 1]$ using $\kappa_2 = 0.07$. The initial estimates are set near the reference solutions and the process and measurement noise covariances are kept the same as the previous test case.

The location of the measurement signals are shown to have an effect on the quality of the estimation, as shown in Fig. 3. Here, both the domain estimates and κ estimates are shown. Representative cases of good and poor estimates are presented to demonstrate how widely the results can vary. The most significant cause of the poor estimation for

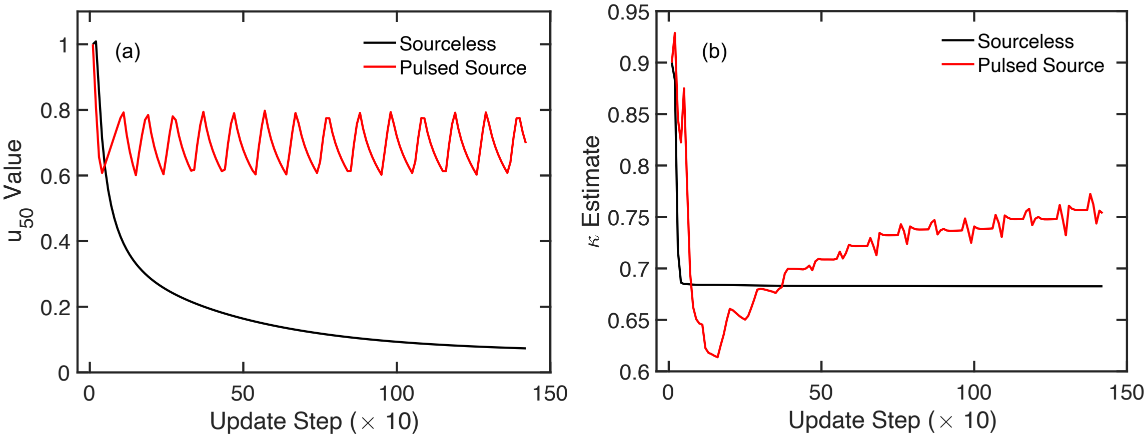

Fig. 2 An example of the pulsed source (pulsed Q_s) versus sourceless ($Q_s = 0$) diffusion tests where Q_s is the source term. (a) The value at the center of the domain, u_{50}, over the course of the simulation for the sourceless diffusion (black) and the pulsed diffusion (red). (b) The estimated thermal conductivity coefficient for the sourceless and pulsed diffusion cases.

the $x = 0.3, 0.7$ measurement location case, as shown using the red solid like in Fig. 3, is due to the incorrect initial condition for the domain. If the same test is run with a correct initial pulse rather than a zero condition, the resulting estimate is significantly closer to the reference solution. The requirement for the EKF to recognize the discontinuous initial pulse of the domain proves challenging when the measurement signals lie outside of the initial pulse width due to the time taken for the system to diffuse. The solution with both measurement conditions inside of the initial pulse, $x = 0.4, 0.6$, shown with the blue dashed line in Fig. 3, yields a significant improvement in the estimation of the overall domain, with only the boundary values beginning to diverge from the reference solution. Though the larger κ_1 value on the left hand side of the domain is overestimated, likely due to the lag in the ability of the EKF to catch the reference dynamics combined with the noise covariances, the smaller κ_2 is estimated almost perfectly.

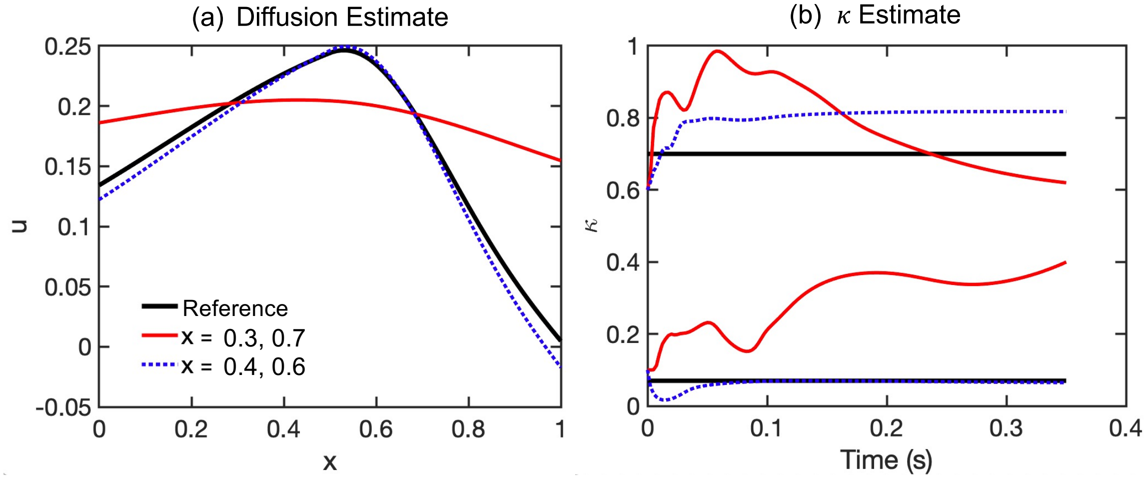

Fig. 3 The estimation results for (a) the diffusing solution and (b) the κ estimates for two unknowns and two measurement signals. The $\kappa = 0.7$ value reference solution corresponds to the left hand side of the domain, while the $\kappa = 0.07$ value is used for the right hand side of the diffusion solution. Note that both plots use the same legend.

VI. Initial Studies using a Fluid Hall Effect Thruster Model

Having applied the EKF to a drift and diffusion representative test case, the EKF is applied to a Hall effect thruster based on a one-dimensional quasineutral drift-diffusion (QDD) fluid model [16]. This model uses a quasineutral assumption for the plasma, a drift-diffusion approximation for the electrons, and accounts only for singly charged ions.

A. Fluid Hall Effect Thruster Model Setup

The conservation equations for mass, momentum, and energy can initially be written as

$$\frac{\partial n}{\partial t} + \nabla \cdot (n\boldsymbol{u}) = S, \tag{7a}$$

$$\frac{\partial}{\partial t}(mn\boldsymbol{u}) + \nabla(mn\boldsymbol{u}.\boldsymbol{u} + p) = q(\boldsymbol{E} + \boldsymbol{u} \times \boldsymbol{B}) + \nabla\tau + \boldsymbol{R}, \tag{7b}$$

$$\frac{\partial}{\partial t}(n\epsilon) + \nabla \cdot (n\boldsymbol{u}\epsilon + p\boldsymbol{u}) = \nabla \cdot \boldsymbol{Q} + qn\boldsymbol{u} \cdot \boldsymbol{E} + S_{elas} - S_{inelas} + \Phi, \tag{7c}$$

where n is the number density, $\boldsymbol{u}$ is the bulk velocity, η is the mean energy, S is the source for particle density, p is the pressure tensor, $\boldsymbol{R}$ is the momentum transfer due to collisions, q is the heat flux vector, and S_{elas}, S_{inelas}, and Φ are energy exchange due to various types of collisions. For the ion continuity equation, the source term can be written as $S_{ion} = n_e \nu_{ion}$ to directly account for the effects of ionization based on a specific rate coefficient obtained from tabulated data generated by BOLSIG+ in the model [17].

The drift-diffusion approximation, assuming one axial direction, can be simplified by also assuming that the transient and inertial terms are neglected since the model assumes electrons are at steady-state within the ion characteristic time and move at low Mach numbers. This leads to a pair of equations to capture the electron transport as

$$\Gamma_{e,x} = n_e u_{e,x} = -\mu_{e,\perp}\left(n_e E_\perp + \frac{1}{e}\frac{\partial p_e}{\partial x_\perp}\right), \tag{8a}$$

$$\Gamma_{e,y} = n_e u_{e,y} = n_e u_{e,x}\Omega, \tag{8b}$$

where the cross-field electron mobility is considered to be $\mu_{e,\perp} = \mu_{\perp,clas} + \mu_{\perp,ano}$, the classical contribution to mobility is $\mu_{\perp,clas} = e/m_e \nu_m (1 + \Omega^2)^{-1}$, the anomalous contribution to mobility is $\mu_{\perp,ano} = \alpha/B$, the Hall parameter is defined as $\Omega = \omega_B/\nu_{m,e}$ based on the electron gyrofrequency $\omega_B = qB/m_e$, the momentum transfer collision frequency is ν_m, α is an empirical coefficient for the anomalous electron transport, n_e is the number density of electrons, and p_e is the electron pressure which can be solved using the ideal gas law with an isotropic assumption.

The quasineutral assumption results in the use of a charge conservation equation to solve the electrostatic electric field. This equation can be written by taking the difference between the ion and electron conservation equations and assuming only electron-impact ionization from the ground state neutral atom to singly charged ions. Coupling this with the quasineutral assumption via the electron flux, allows the potential to be solved as

$$\frac{\partial \Gamma_{e,x}}{\partial x} = \frac{\partial}{\partial x}\left(\mu_{e,\perp} n_e \frac{\partial \phi}{\partial x} - \frac{\mu_{e,\perp}}{e}\frac{\partial p_e}{\partial x}\right) = \frac{\partial \Gamma_{i,x}}{\partial x}, \tag{9}$$

which is a second-order partial differential equation for the electrostatic potential, ϕ, written in the cross-field direction. Note that the electric field is $\boldsymbol{E} = -\nabla\phi$. This equation can be solved using a tridiagonal matrix solver with Dirichlet and Neumann boundary conditions.

A further consequence of the quasineutral assumption is that the anode sheath is unable to be resolved. This study uses an ion-attracting, electron-repelling sheath that assumes a half-Maxwellian distribution of electrons. The sheath potential at the anode can be calculated by

$$-\Gamma_{i,a} + \frac{1}{4} n_{e,a}\sqrt{\frac{8k_B T_{e,a}}{\pi m_e}}\exp\left(-\frac{eV_a}{k_B T_{e,a}}\right) = \frac{j_d}{e}, \tag{10}$$

where j_d is the net current density and V_a is the anode sheath potential used as a boundary condition of Eq. (9). The second boundary condition assumes $\phi = 0$ at the quasineutral electron-injection plane at the cathode. The model interface quantities at the anode are denoted with a subscript a and are solved by extrapolating the values from the cell centers.

The elastic energy loss is negligible in HET discharge plasmas as the electron temperature is typically larger than 5 eV where inelastic collisions become dominant electron energy loss mechanisms. Thus, an alternative to Eq. (7c) for calculating the electron energy is to solve the internal energy equation by subtracting the energy equation obtained from the conservation of momentum from the total energy equation, Eq. (7c). The resulting equation is solved using a second-order implicit Crank-Nicolson scheme to integrate the left hand side in time while the right hand side is solved explicitly using a tridiagonal solver.

The ion pressure can be solved with the ion density and momentum in a coupled fashion to reduce numerical oscillations. The electric field can be shown to be dependent on the ion density, leading to a nonlinear coupling between the electron pressure contribution with the inviscid flux in the ion momentum equation. For this coupling, the ion momentum equation is written for non-magnetized, collisionless ions as

$$\frac{\partial(n_i \boldsymbol{u}_i)}{\partial t} + \nabla\left(n_i \boldsymbol{u}_i \boldsymbol{u}_i + \frac{p_i}{m_i}\right) = \frac{e}{m_i} n_i \boldsymbol{E}.$$

This ion momentum equation is written by substituting the functional form of E to obtain

$$\frac{\partial(n_i u_i)}{\partial t} + \nabla\left(n_i u_i u_i + \frac{p_i + p_e}{m_i}\right) = -\frac{e n_i u_e}{m_i \mu_\perp}, \tag{11}$$

a modified ion momentum equation for the electron-pressure coupled method. Note that the right hand side is a function of $\boldsymbol{u}_e$ but recovers the electric field in the region where the effect of diffusion flux is negligible. A Steger-Warming flux vector splitting scheme is used to evaluate the left hand side of the ion conservation equations based on the inviscid Euler formulation. Further detail of the method can be found in Ref. 16.

B. Estimating the Electron Mobility Parameter

Initial efforts to incorporate the extended Kalman filter with QDD lead to simulations that continually failed. The original setup of the state vector and propagation scheme proved riddled with numerical artifacts as well as complex physical relations leading to unstable solutions. While this work is being reconsidered, the presented work demonstrates a simpler approach. A one-equation update of the electron mobility is used to study the sensitivity of the system to changes in the electron mobility, as a less-intrusive imitation of the effect of the EKF. By providing the QDD model with a measurement discharge current value, an equation for the discharge current,

$$I_d = e(n_i u_i - n_e u_e), \tag{12}$$

can be re-written to solve for the electron mobility parameter, $\mu_\perp$, by substituting the electron velocity with

$$u_e = -\mu_\perp\left(E + \frac{1}{e n_e}\frac{\partial p_e}{\partial x}\right).$$

This equation can be solved for every cell-interface value of the mobility when the measurement signal arrives every 0.5 μs. The electron mobility is solved on the cell-interfaces using Eq. (12) and a simple averaging scheme is used to alternate between cell-interface and cell-center values.

Numerical artifacts are seen to arise from the simple averaging scheme used in the model to transition between cell-center and cell-interface values. When supplying a constant measurement signal, the discharge current is shown to oscillate around the desired solution due to the resulting non-constant mobility in time, as demonstrated in Fig. 4(a). The updated values do not match the steady-state mobility to double precision, leading to instabilities in the state of the plasma that create oscillations in the discharge current. Furthermore, updating the mobility across the entire domain can lead to discontinuities that negatively affect the state of the plasma. The near-anode region is highly sensitive to the update equation, quickly breaking down into large oscillations, as demonstrated in Fig. 4(b). These oscillations were traced back to the electric field, pointing towards the construction of the anode sheath potential as a likely source of uncertainty.

Using this knowledge, specific regions of the domain were allowed to update while others were held constant. This was either performed in accordance with the three-region model proposed by Ref. 4, by selecting only ten cells, or selecting only five cells to be updated. The exit and plume regions are able to be updated, but any of the domain within the channel quickly grows to impossibly large values, causing the simulation to fail as demonstrated in Fig. 4(b). Regardless of the region, the updated mobility is seen to diffuse over time until it reaching some steady value based

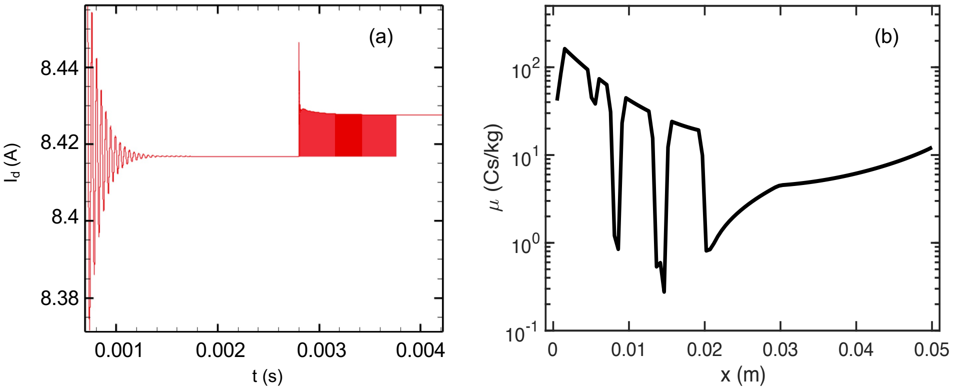

Fig. 4 Example of how imperfections in the steady-state mobility solution leads to (a) oscillations in the discharge current and (b) the electron mobility near the anode.

on how much of the domain is allowed to update. A selection of these results are shown in Fig. 5. Figure 5(a) shows the original steady-state solution as compared to Figure 5(b) where the channel exit and plume (e.g., $x > 0.2$ m) were allowed to update and Figure 5(c) where the entire domain was allowed to update. The steady state reached by the mobility value in the case of the plume update still yields an oscillatory discharge current solution that does not match the original steady-state solution. For the case of the entire domain updating, the declining mobility parameter reduces all plasma in the domain and causes an immediate, and over-exaggerated, need to increase the mobility, as shown in Fig. 5(c). Such a discontinuous jump in value across the domain quickly leads to simulation failure.

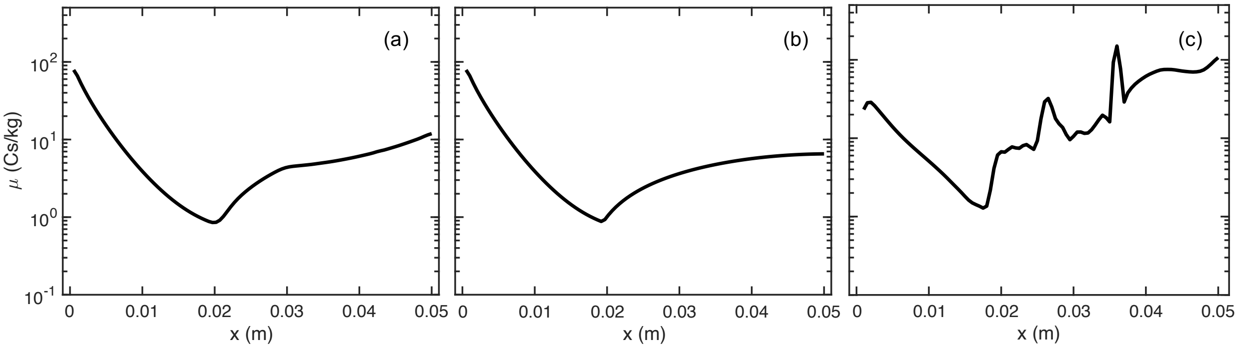

Fig. 5 A selection of electron mobility solutions using the one-equation update. (a) The original, steady-state solution of the electron mobility. (b) The electron mobility if the channel exit and plume cell values are updated, $x \geq 0.02m$. (c) The electron mobility if all cell values are updated.

These results indicate that further consideration must be taken into the setup of this problem. The idea to use an update in the mobility parameter may be insufficient to dictate the state of the system overall, as cited by some observability concerns related to extended Kalman filters [12]. A more stringent averaging technique may be required to reduce numerical artifacts in the model as values are transitioned from cell-center to cell-interface. Specific, physical limitations may be required in the near-anode region to mitigate the oscillations that arise based on considerations such as the anode sheath potential [18]. Isolating the mobility further into its anomalous and classical components may also alleviate some of the numerical discrepancies caused by updating the entire mobility value.

VII. Conclusion

An extended Kalman filter (EKF) is applied to two different one-dimensional models to demonstrate its capabilities for future use with Hall effect thruster models. The EKF is shown to reconstruct the initial domain of a sinusoidal linear advection scheme as well as estimate thermal diffusion coefficients in a thermal diffusion testcase. Both of these tests are imperative to study before applying the EKF to a Hall effect thruster to ensure that the EKF can reasonably estimate quantities such as the electron mobility. Current work is focused on constructing and verifying a one-dimensional Hall effect thruster model based on a quasi-neutral drift-diffusion approximation such that the EKF can be applied. The challenges of this application result from a lack of understanding of best practices for particular limitations on the EKF as applied to as complex of a model as Hall effect thruster physics. Initial tests using a direct-update method have shown the challenges faced with using an extended Kalman filter in a significantly more complex physics-based model. Future work is required to identify physical constraints to improve estimation results or to study alternative estimation techniques.

Acknowledgments

This work was supported by the NDSEG Fellowship program. The authors would like to acknowledge the Air Force Office of Science Research under Grant No. FA9550-21-1-0433, and NASA through the Joint Advanced Propulsion Institute, a NASA Space Technology Research Institute under Grant No. 80NSSC21K1118,

References

[1] Sydorenko, D., Smolyakov, A., Kaganovich, I., and Raitses, Y., "Modification of Electron Velocity Distribution in Bounded Plasmas by Secondary Electron Emission," *IEEE Transactions on Plasma Science*, Vol. 34, No. 3, 2006, pp. 815–824.

[2] Lafleur, T., Baalrud, S. D., and Chabert, P., "Theory for the anomalous electron transport in Hall effect thrusters. II. Kinetic model," *Physics of Plasmas*, Vol. 23, No. 5, 2016, p. 053503. https://doi.org/10.1063/1.4948496.

[3] Koo, J. W., and Boyd, I. D., "Modeling of anomalous electron mobility in Hall thrusters," *Physics of Plasmas*, Vol. 13, No. 3, 2006, p. 033501. https://doi.org/10.1063/1.2172191.

[4] Hofer, R. R., Katz, I., Mikellides, I. G., Goebel, D. M., Jameson, K. K., Sullivan, R. M., and Johnson, L. K., "Efficacy of Electron Mobility Models in Hybrid-PIC Hall Thruster Simulations," AIAA 2008-4924, Hartford, CT, 2008.

[5] Mikellides, I. G., Ortega, A. L., Katz, I., and Jorns, B. A., "Hall2De Simulations with a First-principles Electron Transport Model Based on the Electron Cyclotron Drift Instability," Salt Lake City, UT, 2016.

[6] Jorns, B., "Predictive, data-driven model for the anomalous electron collision frequency in a Hall effect thruster," *Plasma Sources Science and Technology*, Vol. 27, No. 10, 2018, p. 104007. https://doi.org/10.1088/1361-6595/aae472.

[7] Brunton, S. L., Proctor, J. L., and Kutz, J. N., "Discovering governing equations from data by sparse identification of nonlinear dynamical systems," *Proceedings of the National Academy of Sciences*, Vol. 113, No. 15, 2016, pp. 3932–3937. https://doi.org/10.1073/pnas.1517384113.

[8] Greve, C. M., Hara, K., Martin, R. S., Eckhardt, D. Q., and Koo, J. W., "A data-driven approach to model calibration for nonlinear dynamical systems," *Journal of Applied Physics*, Vol. 125, No. 24, 2019, p. 244901. https://doi.org/10.1063/1.5085780.

[9] Greve, C. M., and Hara, K., "Estimation of plasma properties using an extended Kalman filter with plasma global models," *Journal of Physics D: Applied Physics*, Vol. 55, No. 25, 2022, p. 255201. https://doi.org/10.1088/1361-6463/ac5c1c.

[10] Ljung, L., "Asymptotic behavior of the extended Kalman filter as a parameter estimator for linear systems," *IEEE Transactions on Automatic Control*, Vol. 24, No. 1, 1979, pp. 36–50.

[11] Bolognani, S., Tubiana, L., and Zigliotto, M., "Extended Kalman filter tuning in sensorless PMSM drives," *IEEE Transactions on Industry Applications*, Vol. 39, No. 6, 2003, pp. 1741–1747. https://doi.org/10.1109/TIA.2003.818991.

[12] Crassidis, J., and Junkins, J., *Optimal Estimation of Dynamic Systems*, Chapman and Hall, 2004.

[13] Bavdekar, V. A., Deshpande, A. P., and Patwardhan, S. C., "Identification of process and measurement noise covariance for state and parameter estimation using extended Kalman filter," *Journal of Process Control*, Vol. 21, No. 4, 2011, pp. 585–601. https://doi.org/10.1016/j.jprocont.2011.01.001.

[14] Evensen, G., "Using the extended Kalman filter with a multilayer quasi-geostrophic ocean model," *Journal of Geophysical Research: Oceans*, Vol. 97, No. C11, 1992, pp. 17905–17924.

[15] Yanou, A., Hosoya, N., Wada, K., Minami, M., and Matsuno, T., "Estimation of thermal conductivity for model with radiative heat transfer by extended Kalman filter," *2016 IEEE 21st International Conference on Emerging Technologies and Factory Automation (ETFA)*, 2016, pp. 1–4. https://doi.org/10.1109/ETFA.2016.7733670.

[16] Hara, K., Kaganovich, I. D., and Startsev, E. A., "Generation of forerunner electron beam during interaction of ion beam pulse with plasma," *Physics of Plasmas*, Vol. 25, No. 1, 2018, p. 011609. https://doi.org/10.1063/1.5002688.

[17] Hagelaar, G. J. M., and Pitchford, L. C., "Solving the Boltzmann equation to obtain electron transport coefficients and rate coefficients for fluid models," *Plasma Sources Science and Technology*, Vol. 14, No. 4, 2005, p. 722.

[18] Hara, K., Sekerak, M. J., Boyd, I. D., and Gallimore, A. D., "Perturbation analysis of ionization oscillations in Hall effect thrusters," *Physics of Plasmas*, Vol. 21, No. 12, 2014, p. 122103. https://doi.org/10.1063/1.4903843.